

# Lattice dynamics and spin-phonon coupling in the kagome spin ice HoAgGe

Shangfei Wu,<sup>1,\*</sup> Lingxiao Zhao,<sup>2</sup> Wei Song,<sup>2</sup> Mingshu Tan,<sup>3</sup> Feng Jin,<sup>4</sup> Tianping Ying,<sup>4</sup> Jia-Xin Yin,<sup>2</sup> and Qingming Zhang<sup>3,4,†</sup>

<sup>1</sup>*Beijing Academy of Quantum Information Sciences, Beijing 100193, China*

<sup>2</sup>*Department of Physics, Southern University of Science and Technology, Shenzhen, China*

<sup>3</sup>*School of Physical Science and Technology, Lanzhou University, Lanzhou 730000, China*

<sup>4</sup>*Beijing National Laboratory for Condensed Matter Physics, Institute of Physics, Chinese Academy of Sciences, Beijing 100190, China*

(Dated: February 24, 2025)

We employ polarization-resolved Raman spectroscopy and first-principles phonon calculations to study the lattice dynamics and spin-phonon coupling in the kagome spin ice compound HoAgGe. Upon cooling, HoAgGe shows transitions from a nonmagnetic state at 300 K to a partially magnetic-ordered phase below  $T_2 = 11.6$  K, eventually reaching a fully-magnetic ordered phase below  $T_1 = 7$  K. We detect eight of ten Raman-active phonon modes at room temperature, with frequencies consistent with first-principles phonon calculations. We find that the low-energy phonon modes harden upon cooling, soften slightly below  $T_2$ , and finally harden again below  $T_1$ , suggesting finite spin-phonon coupling in HoAgGe. Furthermore, one high-energy mode at  $185 \text{ cm}^{-1}$  with  $E'$  symmetry exhibits a Fano lineshape due to electron-phonon coupling. Our Raman results establish finite spin-phonon coupling and electron-phonon coupling in the magnetic phase of HoAgGe, providing a foundation for future studies of the novel field-induced phases at low temperatures in HoAgGe.

## I. INTRODUCTION

The kagome lattice is a model system to study the electronic and magnetic properties [1]. Especially, the corner-shared triangle network of the kagome lattice is an ideal platform to study the geometrical frustration, which leads to novel phenomena such as quantum spin liquid, spin ice, and macroscopic degeneracy in the ground states without long-range magnetic ordering [2–4]. Spin ice, the local moments replicating the frustration seen in the arrangement of hydrogen ions in frozen water, has been a focus in modern condensed matter physics. The study of these materials has introduced a variety of fascinating concepts of significant interest. At low energies, these materials exhibit an emergent gauge field, and their excitations manifest as magnetic monopoles, which result from the fractionalization of the microscopic spin degrees of freedom [5–8]. Khomskii *et al.* proposed that in spin ice compounds, magnetic monopoles should be accompanied by electric dipoles [9, 10]. The association of electric dipoles with magnetic monopoles allows for the study and manipulation of these exotic monopoles using electric fields, thus providing a way for practical applications [10, 11]. This proposal is confirmed in a quantum spin ice candidate  $\text{Tb}_2\text{Ti}_2\text{O}_7$  which hosts giant spin-lattice (spin-phonon) coupling [12–16] in a Raman scattering experiment [17].

Recently, a kagome spin ice compound exhibiting a fully-ordered ground state has been established in HoAgGe [18]. HoAgGe is a part of the RAgGe (R=Tb-Lu) series, characterized by ZrNiAl-type intermetallics with a noncentrosymmetric  $P\bar{6}2m$  space

group. In this structure, rare-earth ions form a distorted two-dimensional kagome lattice of corner-sharing triangles [Fig. 1(a)] [19]. Each  $\text{Ho}^{3+}$  atom in HoAgGe has ten  $4f$  electrons with ground state of  $^5I_8$ . From the Curie-Weiss fit of the magnetic susceptibility data, an effective magnetic moment  $m_{\text{eff}} = 10.6 \mu_B$  is reported. The system adheres to two-dimensional ice rules defined for in-plane Ising-like classical spins on the kagome lattice, which results in local configurations of two-in-one-out or one-in-two-out spin arrangements on the triangles. The spin-ice state evolves from a nonmagnetic state at room temperature to a partially magnetic-ordered state at  $T_2 = 11.6$  K [Fig. 1(c)], and finally to a fully magnetic-ordered phase at  $T_1 = 7$  K [Fig. 1(d)]. These transitions are also visible in the  $c$ -axis resistivity measurement, with a sharp drop at  $T_2$  and a kink-like feature at  $T_1$  [Fig. 1(b)] [18, 20]. With the magnetic field along the kagome plane, it is noted that the magnetic structures at magnetization plateaus can be derived from the ground state by reversing certain  $\text{Ho}^{3+}$  spins with Ising-like anisotropy, while still following the ice rule [18]. At these magnetization plateaus, it is reported that there exist vanishing hysteresis in the field dependence of the magnetization at low temperatures, but finite hysteresis in the field-dependent anomalous Hall conductivity [21]. Furthermore, at low temperatures in the spin ice state, scanning tunneling microscope measurements reveal a pair of pronounced dips in the local tunneling spectrum at symmetrical bias voltages with negative intensity values, indicating an inelastic tunneling signal linked to spin ice magnetism [22]. The Ising-like  $\text{Ho}^{3+}$  spin reversals induced by the in-plane magnetic field potentially generate magnetic monopole and anti-monopole pairs, along with the emergent electric dipoles attached to these magnetic monopoles [9, 10]. One important ingredient for such phenomena is to have spin-lattice coupling or

\* wusf@baqis.ac.cn

† qmzhang@iphy.ac.cn

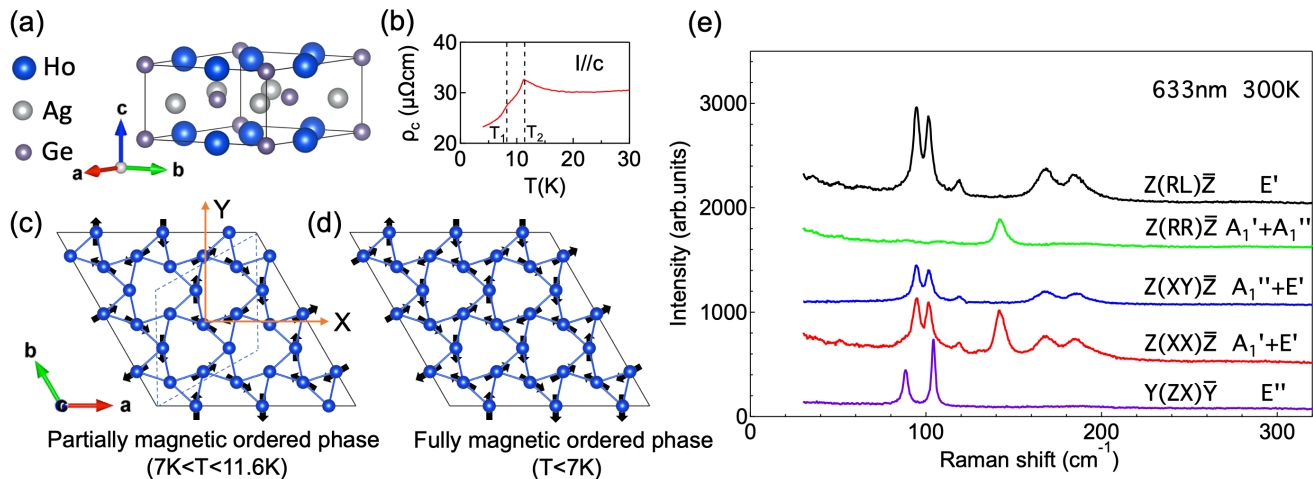


FIG. 1. (a) Crystal structure of HoAgGe. (b)  $T$ -dependence of  $c$ -axis resistivity  $\rho_c$  of HoAgGe. The dashed lines mark the partially magnetic ordered phase transition at  $T_2 = 11.6$  K and the fully magnetic ordered phase transition at  $T_1 = 7$  K. (c)-(d) Illustration of the magnetic structure for HoAgGe in the partially-magnetic-ordered phase ( $T_1 < T < T_2$ ) and fully-magnetic-ordered phase ( $T < T_1$ ), respectively. Ag and Ge atoms are omitted for simplification purpose. The black arrows denote the spin directions, the dashed lines in panel (c) denote the  $\sqrt{3} \times \sqrt{3}$  magnetic unit cell, and the black arrows in panel (c) denote the definitions of the  $X$  and  $Y$  directions. (e) Raman spectra in the  $XX$ ,  $XY$ ,  $RR$ ,  $RL$ , and  $ZX$  scattering geometries at 300 K recorded by a 633 nm laser line.

spin-phonon coupling in this system. However, the lattice dynamics and the estimate of the spin-phonon coupling across these peculiar magnetic phase transitions in HoAgGe are not available in the current literature.

In this paper, we use polarization-resolved Raman spectroscopy and first-principles phonon calculations to investigate the lattice dynamics and spin-phonon coupling in the kagome spin ice compound HoAgGe. We detect eight out of ten Raman-active phonon modes at room temperature. The experimental phonon frequencies are consistent with first-principles phonon calculations. As the temperature drops, the low-energy phonon modes harden due to anharmonic phonon decay, soften slightly below  $T_2$ , and finally harden again below  $T_1$ , indicating the presence of finite spin-phonon coupling in HoAgGe. Additionally, an  $E'$ -symmetry mode at  $185\text{ cm}^{-1}$  shows Fano lineshape due to finite electron-phonon coupling. The Raman results in the present study confirm the existence of finite spin-phonon and electron-phonon coupling in the magnetic phase of HoAgGe, encouraging further research into the novel field-induced phases at low temperatures in this material.

## II. METHODS

*Single crystal preparation and characterization* – Single crystals of HoAgGe were grown by using the Ag-Ge-rich self-flux method as described in detail in Ref. [18]. These samples were characterized by electric transport and magnetic susceptibility measurements at zero magnetic field. The extracted fully-magnetic-ordered

phase transition temperature is  $T_1 = 7$  K, and the partially magnetic-ordered phase transition temperature is  $T_2 = 11.6$  K.

The as-grown HoAgGe single crystal is sliced and meticulously polished to expose its  $(1\ 0\ 0)$  and  $(0\ 0\ 1)$  crystallographic planes. A strain-free area for Raman scattering measurement is examined by a polarized optical image. The strain-free area is further examined by comparing the phonon linewidth obtained on the as-grown  $(0\ 0\ 1)$  crystallographic plane and the polished  $(0\ 0\ 1)$  crystallographic plane. We did not find any noticeable polishing-induced linewidth broadening.

*Raman scattering measurements* – Raman-scattering experiments were performed with a Horiba Jobin-Yvon LabRAM HR evolution spectrometer. One notch filter and two Bragg filters were used in the collection optical path to clean the laser line from the backscattered light. The polished HoAgGe sample was positioned in a closed-cycle-helium-gas-exchange cryostat (AttoDRY 2100), which allows for cooling down to the base temperature 1.8 K. The Raman measurements were mainly performed using a HeNe laser line at 632.8 nm (1.96 eV) in a backscattering geometry. The excitation laser beam was focused into a spot of  $5\ \mu\text{m}$  diameter, with an incident power less than 0.3 mW. Linear and circular polarizations were used in this study to distinguish the symmetry of the Raman modes. Spectra were recorded with a  $1800\text{-mm}^{-1}$  grating and liquid-nitrogen-cooled CCD detector. The instrumental resolution was maintained better than  $0.75\text{ cm}^{-1}$  (full-width at half maximum). All linewidth data presented were corrected for the instrumental resolution. The temperatures shown in this paper were cor-

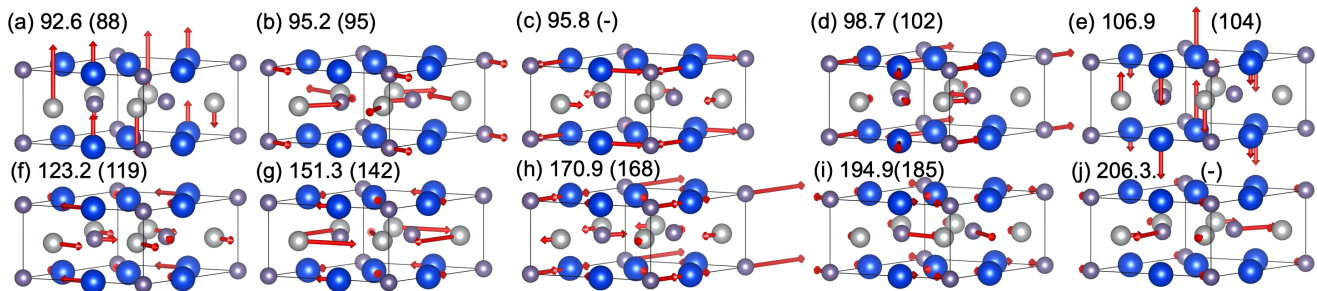


FIG. 2. Major lattice vibration patterns for the Raman-active modes of HoAgGe. The DFT calculated mode frequencies for each mode are shown in each panel while the experimental values are shown in the parentheses. The units are in  $\text{cm}^{-1}$ .

rected for laser heating (Appendix A).

The Raman spectra were recorded from the  $ab$  (0 0 1) and (1 0 0) surface for scattering geometries denoted as  $\mu\nu = XX, XY, RR, RL$ , which is short for  $Z(\mu\nu)\bar{Z}$  in Porto's notation ( $ZX$  is short for  $Y(ZX)\bar{Y}$ ), where  $X$  and  $Y$  denote linear polarization parallel and perpendicular to the crystallographic  $a$  axis, respectively [Fig. 1(c)]. The  $Z$  direction corresponds to the  $c$ -axis direction perpendicular to the (0 0 1) plane. Five scattering geometries were employed to probe excitations in different symmetry channels of HoAgGe. The relationship between the scattering geometries and the symmetry channels could be found in Table I.

*First-principles calculations* – Density functional theory (DFT) calculations for HoAgGe were conducted using the Quantum Espresso code [23, 24]. The exchange and correlation energies use the Perdew-Burke-Ernzerhof form of the generalized-gradient approximation [25]. The ground-state electronic structure was ascertained through the projector-augmented wave method. A plane wave basis cutoff of 120 Ry and charge density cutoff of 800 Ry were employed, and the Monkhorst-Pack  $k$ -point grid was configured to be  $8 \times 8 \times 12$ . The lattice structure was thoroughly relaxed until the total energy and forces acting on atoms dropped below  $10^{-8}$  Ry/atom and  $10^{-8}$  Ry/Bohr, respectively. The phonon dispersion of HoAgGe was calculated using Scalar-Relativistic density-functional perturbation theory (DFPT) with fully relativistic pseudopotentials from the Pseudo-Dojo library [26]. Phonopy [27] was utilized

TABLE I. The relationship between the scattering geometries and the symmetry channels for HoAgGe at zero magnetic field.  $A'_1$ ,  $A''_1$ ,  $E'$  and  $E''$  are the irreducible representations of the  $D_{3h}$  point group.

Scattering Geometry	Symmetry Channel ( $D_{3h}$ )
$XX$	$A'_1 + E'$
$XY$	$A''_1 + E'$
$RR$	$A'_1 + A''_1$
$RL$	$E'$
$ZX$	$E''$

to generate Raman dispersion, as well as to perform post-processing on the calculated interatomic forces, thereby yielding the phonon frequencies. The on-site Coulomb interaction  $U$  is not included as it has a negligible effect on the Brillouin-zone center phonon frequencies.

*Group theoretical analysis* – Group theoretical analysis were performed using the tool provided in the Isotropy Software Suite and the Bilbao Crystallographic Server [28–30]. The information for the irreducible representations of point groups and space groups follow the notations of Cracknell, Davies, Miller, and Love [31].

### III. RESULTS AND DISCUSSIONS

#### A. Phonon modes

HoAgGe belongs to the hexagonal structure with space group  $P\bar{6}2m$  (No. 189) (point group:  $D_{3h}$ ) [Fig. 1(a)]. The Ho, Ag, Ge<sup>1</sup> (in the honeycomb layer), and Ge<sup>2</sup> atoms (in the kagome layer) have Wyckoff positions  $3f$ ,

TABLE II. Experimental phonon frequencies at the Brillouin zone center for HoAgGe at 300 K and the phonon frequencies calculated by DFT. All the units are in  $\text{cm}^{-1}$ .

Symmetry	Activity	Maj. Displacement	Cal.	Exp.
$A''_2$	IR	Ho( $z$ ), Ag( $z$ )	86.3	
$E''$	Raman	Ho( $z$ ), Ag( $z$ )	92.6	88
$E'$	IR+Raman	Ag( $xy$ ), Ge( $xy$ )	95.2	95
$A'_1$	Raman	Ho( $xy$ )	95.8	-
$E'$	IR+Raman	Ho( $xy$ ), Ge( $xy$ )	98.7	102
$E''$	Raman	Ho( $z$ )	106.9	104
$A'_2$	-	Ho( $xy$ ), Ag( $xy$ )	107.2	
$E'$	IR+Raman	Ho( $xy$ ), Ag( $xy$ )	123.2	119
$A'_2$	-	Ho( $xy$ ), Ag( $xy$ )	146.4	
$A'_1$	Raman	Ag( $xy$ )	151.3	142
$A''_1$	-	Ho( $xy$ ), Ag( $xy$ )	163.6	
$E'$	IR+Raman	Ge( $xy$ )	170.9	168
$A''_2$	IR	Ge( $z$ )	180.5	
$A''_2$	IR	Ag( $z$ ), Ge( $z$ )	189.3	
$E'$	IR+Raman	Ge( $xy$ )	194.9	185
$E'$	IR+Raman	Ge( $xy$ )	206.3	-

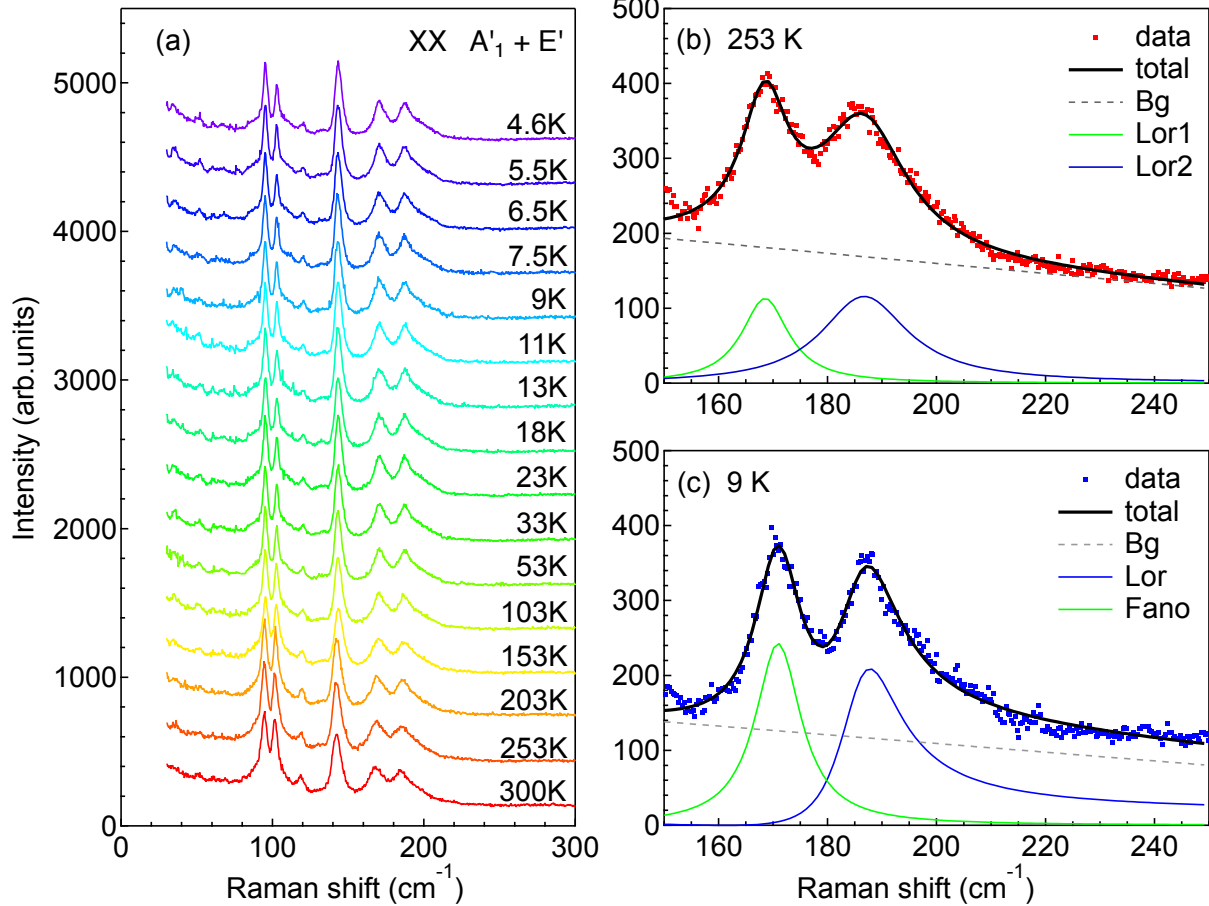


FIG. 3. (a) Temperature dependence of the Raman response in the  $XX$  ( $A_1' + E'$ ) scattering geometry. (b) Raman response for the two modes at 168 and 185  $\text{cm}^{-1}$  at 300 K. The solid black line is a fit using a sum of two Lorentzian functions and a linear background. The dashed line represents the background. The two components are shown in green and blue thin lines. (c) Same as (b) but for 9 K. The solid black line is a fit using a sum of a Lorentzian function, a Fano lineshape, and a linear background.

$3d$ ,  $2d$ , and  $1a$ , respectively. From the group theoretical considerations [28],  $\Gamma$ -point phonon modes of the hexagonal HoAgGe can be expressed as  $\Gamma_{\text{total}} = 2A_1' \oplus 2A_2' \oplus A_1'' \oplus 4A_2'' \oplus 7E' \oplus 2E''$ . Raman active modes are  $\Gamma_{\text{Raman}} = 2A_1' \oplus 6E' \oplus 2E''$ , IR active modes are  $\Gamma_{\text{IR}} = 3A_2'' \oplus 6E'$ , the acoustic mode is  $\Gamma_{\text{acoustic}} = A_2'' \oplus E'$ , and the silent modes are  $\Gamma_{\text{silent}} = 2A_2' \oplus A_1''$ . Note that (1) The inversion symmetry is absent in the point group  $D_{3h}$ . Thus, the  $E'$  modes are both Raman and IR active,  $A_2''$  is IR active while  $A_1'$  is Raman active; (2) Both Ag and Ho sites have  $A_1'$  Raman-active modes while Ge sites have no  $A_1'$  Raman-active modes; (3)  $E'$  modes are accessible from the  $ab$ -plane measurement while  $E''$  modes are accessible from the  $ac$ -plane measurement.

In Fig. 1(e), we show the polarization-resolved Raman response for HoAgGe in five scattering geometries. In the  $XX$  scattering geometry, six phonon modes (95, 102, 119, 142, 168, and 185  $\text{cm}^{-1}$ ) are well resolved which are

$A_1'$  and  $E'$  symmetry modes. The symmetry of these modes can be separated by using the circular polarizations (Table I). The single mode at 142  $\text{cm}^{-1}$  observed in the  $RR$  scattering geometry is assigned to be an  $A_1'$  mode, which is mainly related to the Ag-lattice vibration modes. The rest five modes (95, 102, 119, 168, and 185  $\text{cm}^{-1}$ ) observed in the  $RL$  scattering geometry are assigned to be  $E'$  modes. According to the group-theoretical analysis, two  $A_1'$  modes are expected. The one related to the Ho lattice vibration  $A_1'$  mode is supposed to have a smaller vibration frequency due to the large mass of Ho atom. It might be too weak to be observed. In the  $ZX$  scattering geometry, two modes observed at 88 and 104  $\text{cm}^{-1}$  are assigned to be  $E''$  modes. The phonon frequencies and symmetry of these modes are summarized in Table II. The major lattice vibration patterns for the Raman-active modes of HoAgGe are shown in Fig. 2.

To further understand the lattice dynamics of

HoAgGe, we perform the DFT phonon calculations. We summarize the calculated phonon frequencies and the experimental phonon frequencies at Brillouin zone center in Table II. Overall, the experimentally observed phonon frequencies are consistent with the DFT phonon calculations. We note that two modes predicted by DFT are not detected in the experiments which might be due to the weak Raman intensities.

## B. Temperature dependence

After establishing the Raman modes of HoAgGe at room temperature, we present their temperature dependence.

In Fig. 3(a), we show the temperature dependence of the Raman response in the  $XX$  ( $A'_1 + E'$ ) scattering geometry across the two magnetic phase transitions. All the phonon modes show hardening and narrowing upon cooling. The temperature dependence of the mode frequency and HWHM (half-width at half-maximum) in the nonmagnetic phase shown in Fig. 4 are consistent with the conventional phonon anharmonic decay model [Appendix B]. Notably, as we show in Fig. 3(b), the  $E'$  mode at  $185\text{ cm}^{-1}$  shows symmetric lineshape at  $253\text{ K}$ , which can be modeled by a Lorentzian function. It develops an asymmetric lineshape upon cooling, indicating Fano-type interference lineshape due to finite electron-phonon coupling. The Fano resonance effect originates from a quantum interference between a discrete state (in this case a phonon mode) and an electron continuum, in which the excited eigenstates are a mixture of the discrete and continuum states [32]. The Fano lineshape is described by the equation

$$I(\omega) = A \frac{[q + (\omega - \omega_0)/\Gamma]^2}{1 + [(\omega - \omega_0)/\Gamma]^2}, \quad (1)$$

Where  $A$  represents the amplitude,  $\omega_0$  represents the bare mode frequency,  $\Gamma$  is the HWHM (half-width at half-maximum) of the coupled Fano-shaped mode,  $q$  is inversely proportional to the electron-phonon interaction strength. As we show in Fig. 3(c), a Fano lineshape can model the mode at  $185\text{ cm}^{-1}$  very well with parameters  $\omega_0 = 185.9$ ,  $\Gamma = 6.7$ , and  $q = 3.7$ . The strength of the electron-phonon coupling can be approximately estimated by the parameter  $1/q$ . The temperature dependence of  $1/q$  is shown in the inset of Fig. 4(l). The parameter  $1/q$  increases upon cooling, and it is  $0.27$  at  $9\text{ K}$  for HoAgGe, similar to  $\text{BaFe}_2\text{As}_2$  slightly below the structure phase transition ( $|1/q| \sim 0.35$ ) [33]. The magnitude of  $1/q$  in HoAgGe suggests moderate electron-phonon coupling in the Brillouin zone center.

In Fig. 5, we present the temperature dependence of the peak position, HWHM, and integrated intensity for the Raman modes of HoAgGe upon cooling across the magnetic phase transition. The temperature dependence of the HWHM and the integrated intensity show little

anomalies upon cooling across the magnetic phase transitions. In contrast, the temperature dependence of the phonon frequencies for the  $E'$  mode at  $94$  and  $102\text{ cm}^{-1}$  and the  $A'_1$  mode at  $142\text{ cm}^{-1}$  harden upon cooling to  $T_2$ , then softens below  $T_2$ , and finally harden again below  $T_1$ . The softening of both the  $A'_1$  and  $E'$  modes below  $T_2$  is attributed to a renormalization of phonon energy due to spin-phonon coupling. Especially, the low-energy in-plane  $E'$ -symmetry mode containing mainly Ho lattice vibration modulate the neighboring Ho spin exchange energy, creating a coupling between the Ho lattice vibration mode and the Ho spin ordering. The magnitude of the phonon softening between  $T_1$  and  $T_2$  is about  $0.2\text{ cm}^{-1}$ , which is about  $\delta\omega/\omega = -0.2\%$  for the mode at  $102\text{ cm}^{-1}$ . It is the similar magnitude as the  $E_g$  mode at  $248\text{ cm}^{-1}$  in  $\text{MnF}_2$  ( $-0.5\%$ ) [34],  $E_g$  mode at  $308\text{ cm}^{-1}$  in  $\text{NiF}_2$  ( $-0.3\%$ ) [35], the  $476$  and the  $573\text{ cm}^{-1}$  modes in  $\text{Na}_{0.5}\text{CoO}_2$  ( $-0.2\%$ ) [36].

We could estimate the spin-phonon coupling constant by the shift of phonon frequency across the magnetic phase transitions via

$$\Delta\omega = \omega_p - \omega_p^0 = \lambda \langle \mathbf{S}_i \cdot \mathbf{S}_{i+1} \rangle. \quad (2)$$

Here,  $\langle \mathbf{S}_i \cdot \mathbf{S}_{i+1} \rangle$  denotes a statistical mechanical average for the adjacent spin pairs. The spin-phonon coupling constant  $\lambda$  is proportional to the second derivative of the direct exchange energy with respect to the phonon coordinate. It varies for each phonon and could have either a positive or negative sign depending on the phonon mode. For a detailed comparison between experiment and theory, the  $T$ -dependent  $\langle \mathbf{S}_i \cdot \mathbf{S}_{i+1} \rangle$  can be evaluated by  $S^2\phi(T)$  where  $\phi(T) = |\langle \mathbf{S}_i \cdot \mathbf{S}_{i+1} \rangle|/S^2$ .  $S$  denotes the effective spin quantum number.  $S^2$  can be estimated via the equation  $S^2 = [M/(2\mu_B)]^2$  [36–38], and  $\phi(T)$  can be estimated from the  $T$ -dependence of the integrated intensities for the magnetic Bragg peak ( $1/3\ 1/3\ 0$ ) [18]. At  $4\text{ K}$ , the ordered magnetic moment  $M=7.5\mu_B$  [18], the estimated  $S^2$  is  $14$ . Since  $\phi(7\text{ K}) \sim 0.8$ , and  $\Delta\omega = -0.2 \pm 0.05\text{ cm}^{-1}$  for the  $E'$  mode at  $102\text{ cm}^{-1}$ , the extracted spin-phonon coupling constant  $\lambda \sim -0.02 \pm 0.004\text{ cm}^{-1}$ . This is similar for the modes at  $94$  and  $142\text{ cm}^{-1}$ . The overall spin-phonon coupling constant  $\lambda$  in HoAgGe is about an order of magnitude smaller than those in typical antiferromagnet  $\text{NiF}_2$ ,  $\text{FeF}_2$ , and  $\text{MnF}_2$  where an average  $|\lambda|$  is close to  $0.3 - 0.4$  [34, 35]. It is much smaller than the  $\text{ZnCr}_2\text{O}_4$  compound with a spin-phonon coupling constant of about  $5\text{ cm}^{-1}$  [39]. The small spin-phonon coupling constant in HoAgGe originates from a small phonon softening below the  $T_2$  magnetic phase transition in a classical spin ice compound with a large ordered magnetic moment.

Finally, we discuss the implications of the finite spin-phonon coupling in HoAgGe. Zhao *et al.* reported that the Hall conductivity  $\sigma_{ac}$  change signs at the metamagnetic transitions around  $3\text{ T}$  when magnetic fields are applied parallel to the kagome plane [21]. It is believed to be related to the substantial changes of the band structure near the Fermi energy driven by the magnetic order

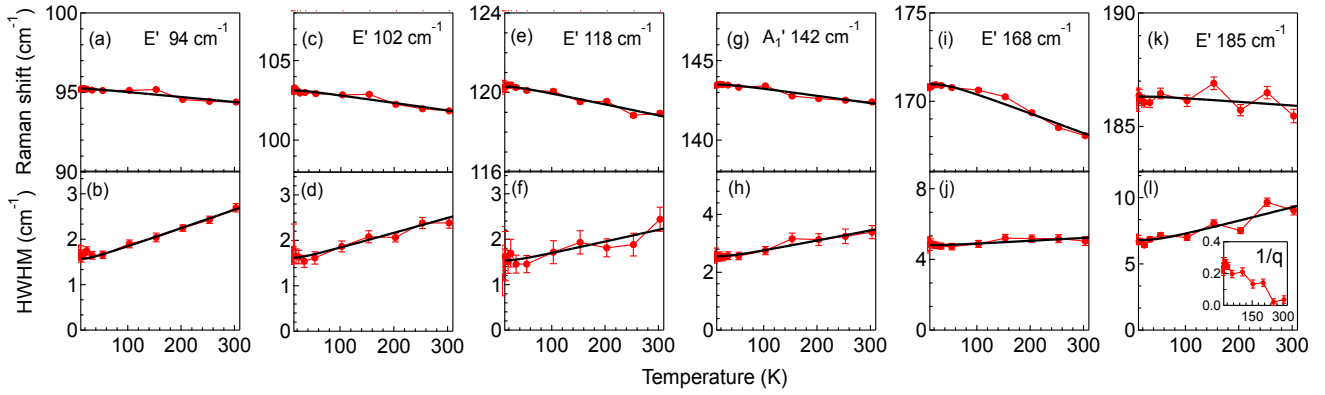


FIG. 4. Fitting of the temperature-dependence of the peak position, HWHM (half-width at half-maximum) for the Raman modes of HoAgGe using the anharmonic phonon decay model above  $T_2$  (Appendix B). (a)-(b) For the mode at  $94 \text{ cm}^{-1}$ . (c)-(d) For the mode at  $102 \text{ cm}^{-1}$ . (e)-(f) For the mode at  $118 \text{ cm}^{-1}$ . (g)-(h) For the mode at  $142 \text{ cm}^{-1}$ . (i)-(j) For the mode at  $168 \text{ cm}^{-1}$ . (k)-(l) For the mode at  $185 \text{ cm}^{-1}$ . The inset of (l) shows the temperature dependence of the Fano model parameter  $1/q$ . The error bars represent one standard deviation.

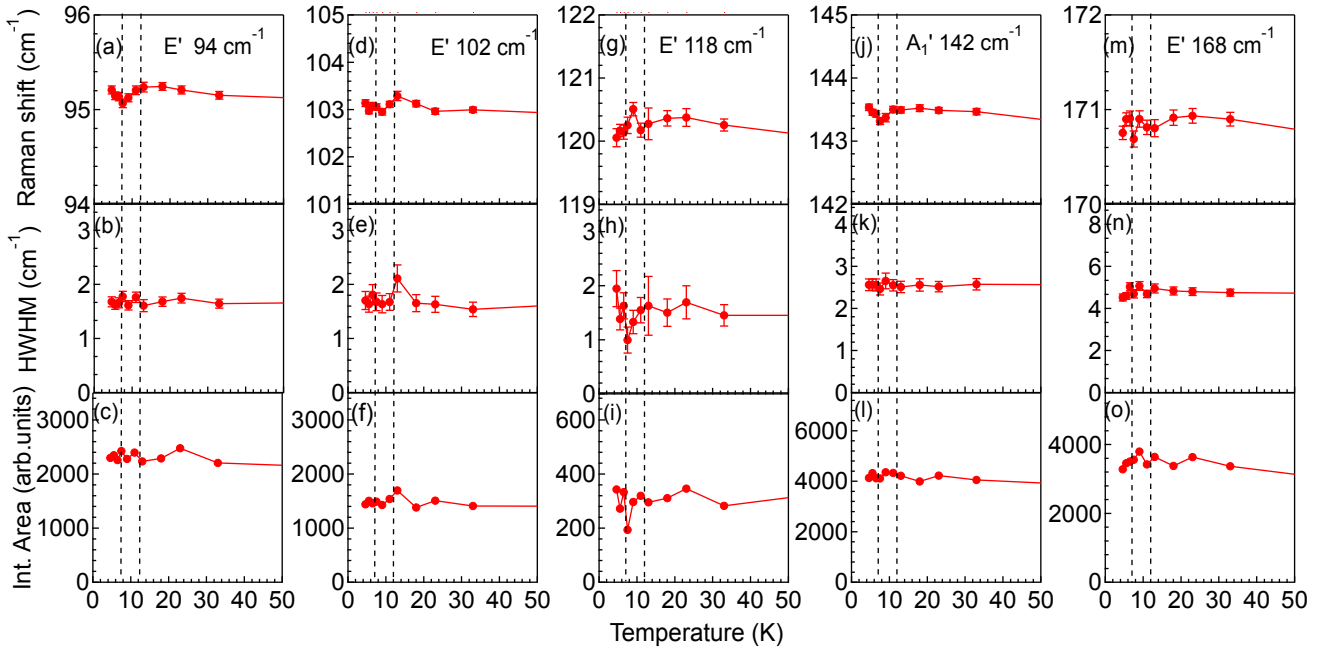


FIG. 5. Temperature dependence of the peak position, HWHM, and integrated intensity for the Raman modes of HoAgGe. (a)-(c) For the mode at  $94 \text{ cm}^{-1}$ . (d)-(f) For the mode at  $102 \text{ cm}^{-1}$ . (g)-(i) For the mode at  $118 \text{ cm}^{-1}$ . (j)-(l) For the mode at  $142 \text{ cm}^{-1}$ . (m)-(o) For the mode at  $168 \text{ cm}^{-1}$ . The error bars represent one standard deviation. The dashed lines mark  $T_1$  and  $T_2$  temperatures.

change [21]. On the presence of finite spin-phonon coupling, the lattice structure in HoAgGe could respond to the magnetic order change, which might account for the band structure change in the metamagnetic transitions. Furthermore, when applying an in-plane magnetic field along the  $b$  axis (*e.g.* 1.5 T) for HoAgGe in the spin ice state below  $T_1$ , part of the spins flip the sign along the line between the corner and the center of the triangles. As a result, the magnetic unit cell changes from hexago-

nal at zero magnetic field to orthorhombic at finite magnetic field [18]. The lattice structure could respond to the new magnetic unit cell on the presence of the spin-lattice coupling, breaking the three-fold lattice rotational symmetry. A similar case was discussed in  $\text{Tb}_2\text{Ti}_2\text{O}_7$  [17]. Thus, the two-fold degenerate  $E'$  and  $E''$  phonon modes in HoAgGe could split into two modes in the orthorhombic magnetic unit cell. Lastly, the magnetic field-induced spin-flips in HoAgGe also motivate to study the potential

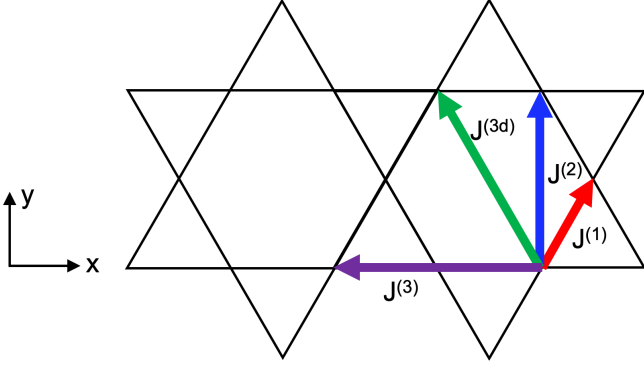


FIG. 6. Illustration of the kagome lattice.  $J^{(1)}$ ,  $J^{(2)}$ ,  $J^{(3)}$ , and  $J^{(3d)}$  represent the first, second, third along the triangle edges, and third along the hexagon diagonal nearest neighbor exchange energies, respectively.

emergent magnetic monopole and anti-monopole pairs, as well as the attached electric dipoles on the presence of finite spin-phonon coupling. While we do not observe such splitting of two-fold degenerate modes and the signatures of the magnetic monopole and anti-monopole pairs because our Raman experiment is performed at 0T, our results of the phonon modes at zero magnetic field and spin-phonon coupling provide a basis for the future study of the kagome spin-ice-related physics in the magnetic field.

Generally speaking, the existence of spin-phonon coupling in the spin-ice system puts additional terms or constraints on the low-energy spin Hamiltonian. For HoAgGe, the low-energy spin Hamiltonian includes Heisenberg exchange couplings up to  $n$ -th nearest neighbors, magnetic dipolar interaction, Zeeman coupling with an external in-plane magnetic field:

$$\begin{aligned}
 H_0 = & J_0 \sum_{\langle ij \rangle^{(1)}} \vec{S}_i \cdot \vec{S}_j \\
 & + Da^3 \sum_{i \neq j} \left[ \frac{\vec{S}_i \cdot \vec{S}_j}{(r_{ij}^0)^3} - \frac{3(\vec{S}_i \cdot \hat{r}_{ij})(\vec{S}_j \cdot \hat{r}_{ij})}{(r_{ij}^0)^3} \right] \quad (3) \\
 & - \vec{h} \cdot \sum_i \vec{S}_i,
 \end{aligned}$$

where  $\vec{S}_i = S\sigma_i\hat{e}_i$  is a local Ising spin,  $\sigma_i = \pm 1$  is the Ising variable,  $\hat{e}_i$  is the local reference direction pointing to the center of the triangle,  $S$  is the spin magnitude.  $J_0$  is the strength of the first nearest-neighbor exchange coupling between site  $i$  and  $j$ ,  $D$  is the strength of the dipolar coupling.  $r_{ij}^0$  is the distance between any pair of spins at site  $i$  and site  $j$ .  $\hat{r}_{ij}$  is the unit vector from site  $i$  to site  $j$ .  $\vec{h} = h_x\hat{x} + h_y\hat{y}$  is the external magnetic field direction in the kagome plane [Fig. 6].

The effects of lattice deformations  $\vec{u}_i$  on the magnetic order have been discussed in the literature in two models:

bond phonon model [40], Einstein site phonon model [41–50]. The bond phonon model assumes that each bond can deform independently which ignores the geometrical constraints [40]. A more realistic phonon model can be described using the independent displacements of each atom at each site, with bond distances derived from these displacements, corresponding to the Einstein site phonon model [41]. Adopting the standard Einstein site phonon model and doing a first order Taylor expansion, the changes to the exchange and dipolar terms of the spin Hamiltonian as a result of atomic displacements can be approximated as linear terms in  $\vec{u}_i$ , which can be integrated out to obtain an effective spin Hamiltonian. Since the spin Hamiltonian Eq. 3 for HoAgGe is equivalent to the planar kagome spin ice model developed in the Ising pyrochlore system under an external magnetic field in the [111] direction where the apical spins are completely aligned with the external magnetic field, we quote the effective spin Hamiltonian following Ref. [43]:

$$\begin{aligned}
 \frac{H_{\text{eff}}}{J_0 S^2} = & \left[ J_{\text{eff}}^{(1)} \sum_{\langle ij \rangle^{(1)}} \sigma_i \sigma_j + J_{\text{eff}}^{(2)} \sum_{\langle ij \rangle^{(2)}} \sigma_i \sigma_j \right. \\
 & + J_{\text{eff}}^{(3)} \sum_{\langle ij \rangle^{(3)}} \sigma_i \sigma_j + J_{\text{eff}}^{(3d)} \sum_{\langle ij \rangle^{(3d)}} \sigma_i \sigma_j \left. \right] \quad (4) \\
 & - \sum_i \sigma_i \left[ \tilde{h}_x (\hat{e}_i)_x + \tilde{h}_y (\hat{e}_i)_y \right]
 \end{aligned}$$

where  $\langle ij \rangle^{(1)}$ ,  $\langle ij \rangle^{(2)}$ ,  $\langle ij \rangle^{(3)}$ , and  $\langle ij \rangle^{(3d)}$  are first, second, third along triangle edges, and third along hexagon diagonal neighbors, respectively [Fig. 6]. The spin-phonon coupling constant is defined as  $\alpha = -\frac{1}{J_0} \frac{\partial J}{\partial r_{ij}} \Big|_{r_{ij}=r_{ij}^0}$ . The dimensionless spin-phonon coupling constant can be defined as  $\lambda' = a\alpha$  ( $a$  is the distance between nearest neighbors). The dimensionless dipolar interaction strength can be defined as  $d = \frac{D}{J_0}$ , and the dimensionless magnetic field can be defined as  $\tilde{h}_t = h_t / (J_0 S)$  with  $t = x, y$ . The effective exchange couplings are given by

$$\begin{aligned}
 J_{\text{eff}}^{(1)} &= -\frac{1}{2} + \frac{7}{4}d - \delta, \\
 J_{\text{eff}}^{(2)} &= -\frac{5}{12\sqrt{3}}d + \delta, \\
 J_{\text{eff}}^{(3d)} &= \frac{1}{8}d \\
 J_{\text{eff}}^{(3)} &= -\frac{5}{32}d + 2\delta,
 \end{aligned} \quad (5)$$

with  $\delta = \frac{S^2}{4k} \left( -\frac{\lambda'}{2} + \frac{21}{4}d \right)^2$  [43]. From these effective exchange energy Eqs. 5, we find that the spin-phonon coupling affects both the first, second, and third neighbor exchange energies.

From the Monte Carlo simulations of HoAgGe [18],  $J^{(1)}$  is estimated to be  $-2$  meV,  $J^{(2)}$  is estimated to be  $0.23$  meV,  $J^{(3)}$  and  $J^{(3d)}$  are estimated to be  $0.127$  meV.

The dipolar interaction has a typical energy scale of  $\sim 0.11$  meV. From our Raman results, the softening of the phonon modes at the magnetic ordering is about  $0.2 \text{ cm}^{-1}$ , corresponding to an energy scale of about  $0.025$  meV. It is about 1% of  $J^{(1)}$ , 10% of  $J^{(2)}$ , 20% of  $J^{(3)}$  and  $J^{(3d)}$ , and 20% of the dipolar energy. While the spin-phonon coupling barely affects  $J^{(1)}$  for HoAgGe, it moderately affects the further nearest neighbor exchange interactions. This may play a role in stabilizing the rich magnetic plateaus observed in HoAgGe [18] according to the kagome spin ice model [43]. More detailed theoretical studies of spin-phonon (spin-lattice) interaction by first-principles calculations [51] or Monte Carlo simulations [43–46, 48] for the kagome spin ice HoAgGe on the quantitative level call for future studies.

#### IV. CONCLUSIONS

In conclusion, we study the lattice dynamics and spin-phonon coupling in the kagome spin ice compound HoAgGe using Raman spectroscopy and first-principles phonon calculations. We detect eight of ten Raman-active phonon modes at 300 K, the frequency of which is in accord with first-principles phonon calculations. Upon cooling, we find that the low-energy phonon modes harden first, but soften slightly below  $T_2$ , and finally harden again below  $T_1$ , suggesting finite spin-phonon coupling in HoAgGe. Furthermore, we find a high-energy  $E'$ -mode at  $185 \text{ cm}^{-1}$  show asymmetric lineshape, indicating finite electron-phonon coupling in this system. The finite spin-phonon coupling and electron-phonon coupling motivate the study of the novel field-induced effects in HoAgGe, for example, spin-flips induced three-fold rotational symmetry breaking in the magnetic unit cell, and emergent electric dipoles attached to the magnetic monopole and anti-monopole pairs.

#### ACKNOWLEDGMENTS

This work was supported by the National Natural Science Foundation of China (Grant No. 12404548 and

No. 12274186), the National Key Research and Development Program of China (Grant No. 2022YFA1402704), the Strategic Priority Research Program of the Chinese Academy of Sciences (Grant No. XDB33010100), and the Synergetic Extreme Condition User Facility (SECUF).

#### Appendix A: Laser heating determination

The laser heating rate, a measure of the temperature increase per unit laser power (K/mW) in the focused laser spot, in the Raman experiments was determined by monitoring the phonon frequency anomalies induced by the magnetic order during the warming-up process with a constant laser power of  $0.3$  mW. The temperature dependence of the phonon frequencies for HoAgGe are shown in Fig. 5. At the cryostat temperature  $8$  K, we detect a phonon anomaly corresponding to the partially magnetic-ordered phase temperature  $T_2=11.6$  K, indicating the laser spot temperature is close to  $T_2$ . Thus, the heating coefficient can be determined via  $8 \text{ K} + 0.3 \text{ mW} * k \approx 11.6 \text{ K}$ . In this way, we have deduced the heating coefficient  $k \approx 12 \pm 1 \text{ K/mW}$ .

#### Appendix B: Anharmonic phonon decay model

In this appendix, we discuss the anharmonic phonon decay model. We fit the temperature dependence of the phonon frequency and HWHM by anharmonic phonon decay model [52, 53]:

$$\omega_1(T) = \omega_0 - C_1 [1 + 2n(\Omega(T)/2)], \quad (\text{B1})$$

$$\Gamma_1(T) = \gamma_0 + \gamma_1 [1 + 2n(\Omega(T)/2)], \quad (\text{B2})$$

where  $\Omega(T) = \hbar\omega/k_B T$ ,  $n(x) = 1/(e^x - 1)$  is the Bose-Einstein distribution function.  $\omega_1(T)$  and  $\Gamma_1(T)$  involves mainly three-phonon decay process where an optical phonon decays into two acoustic modes with equal energy and opposite momentum.

- 
- [1] Itiro Syōzi, “Statistics of Kagome Lattice,” *Progress of Theoretical Physics* **6**, 306–308 (1951).
  - [2] Ian Gilbert, Cristiano Nisoli, and Peter Schiffer, “Frustration by design,” *Physics Today* **69**, 54–59 (2016).
  - [3] C. Broholm, R. J. Cava, S. A. Kivelson, D. G. Nocera, M. R. Norman, and T. Senthil, “Quantum spin liquids,” *Science* **367**, eaay0668 (2020).
  - [4] C. Broholm, R. J. Cava, S. A. Kivelson, D. G. Nocera, M. R. Norman, and T. Senthil, “Quantum spin liquids,” *Science* **367**, eaay0668 (2020).
  - [5] Steven T. Bramwell and Michel J. P. Gingras, “Spin ice state in frustrated magnetic pyrochlore materials,” *Science* **294**, 1495–1501 (2001).
  - [6] C. Castelnovo, R. Moessner, and S.L. Sondhi, “Spin ice, fractionalization, and topological order,” *Annual Review of Condensed Matter Physics* **3**, 35–55 (2012).
  - [7] C. Castelnovo, R. Moessner, and S. L. Sondhi, “Magnetic monopoles in spin ice,” *Nature* **451**, 42–45 (2008).
  - [8] Steven T. Bramwell and Mark J. Harris, “The history of spin ice,” *Journal of Physics: Condensed Matter* **32**, 374010 (2020).



- [9] D. I. Khomskii, “Spin chirality and nontrivial charge dynamics in frustrated Mott insulators: spontaneous currents and charge redistribution,” *Journal of Physics: Condensed Matter* **22**, 164209 (2010).
- [10] D. I. Khomskii, “Electric dipoles on magnetic monopoles in spin ice,” *Nature Communications* **3**, 904 (2012).
- [11] Christoph P. Grams, Martin Valldor, Markus Garst, and Joachim Hemberger, “Critical speeding-up in the magnetoelectric response of spin-ice near its monopole liquid-gas transition,” *Nature Communications* **5**, 4853 (2014).
- [12] I. V. Aleksandrov, B. V. Lidskii, L. G. Mamsurova, M. G. Neigauz, K. S. Pigal’skii, K. K. Pukhov, N. G. Trusevich, and L. G. Shcherbakova, “Crystal field effects and the nature of the giant magnetostriction in terbium dititanate,” *Soviet Journal of Experimental and Theoretical Physics* **62**, 1287 (1985).
- [13] J. P. C. Ruff, Z. Islam, J. P. Clancy, K. A. Ross, H. Nojiri, Y. H. Matsuda, H. A. Dabkowska, A. D. Dabkowski, and B. D. Gaulin, “Magnetoelastics of a Spin Liquid: X-Ray Diffraction Studies of  $\text{Tb}_2\text{Ti}_2\text{O}_7$  in Pulsed Magnetic Fields,” *Phys. Rev. Lett.* **105**, 077203 (2010).
- [14] V. V. Klekovkina, A. R. Zakirov, B. Z. Malkin, and L. A. Kasatkina, “Simulations of magnetic and magnetoelastic properties of  $\text{Tb}_2\text{Ti}_2\text{O}_7$  in paramagnetic phase,” *Journal of Physics: Conference Series* **324**, 012036 (2011).
- [15] T. Fennell, M. Kenzelmann, B. Roessli, H. Mutka, J. Ollivier, M. Ruminy, U. Stuhr, O. Zaharko, L. Bovo, A. Cervellino, M. K. Haas, and R. J. Cava, “Magnetoelastic Excitations in the Pyrochlore Spin Liquid  $\text{Tb}_2\text{Ti}_2\text{O}_7$ ,” *Phys. Rev. Lett.* **112**, 017203 (2014).
- [16] M. Ruminy, S. Guitteny, J. Robert, L.-P. Regnault, M. Boehm, P. Steffens, H. Mutka, J. Ollivier, U. Stuhr, J. S. White, B. Roessli, L. Bovo, C. Decorse, M. K. Haas, R. J. Cava, I. Mirebeau, M. Kenzelmann, S. Petit, and T. Fennell, “Magnetoelastic excitation spectrum in the rare-earth pyrochlore  $\text{Tb}_2\text{Ti}_2\text{O}_7$ ,” *Phys. Rev. B* **99**, 224431 (2019).
- [17] Feng Jin, Changle Liu, Yanfen Chang, Anmin Zhang, Yimeng Wang, Weiwei Liu, Xiaoqun Wang, Young Sun, Gang Chen, Xuefeng Sun, and Qingming Zhang, “Experimental Identification of Electric Dipoles Induced by Magnetic Monopoles in  $\text{Tb}_2\text{Ti}_2\text{O}_7$ ,” *Phys. Rev. Lett.* **124**, 087601 (2020).
- [18] Kan Zhao, Hao Deng, Hua Chen, Kate A. Ross, Vaclav Petříček, Gerrit Günther, Margarita Russina, Vladimir Hutanu, and Philipp Gegenwart, “Realization of the kagome spin ice state in a frustrated intermetallic compound,” *Science* **367**, 1218–1223 (2020).
- [19] S. Baran, M. Hofmann, J. Leciejewicz, B. Penc, M. Ślaski, and A. Szytuła, “Magnetic order in  $\text{RAgGe}$  ( $\text{R}=\text{Gd-Er}$ ) intermetallic compounds,” *Journal of Alloys and Compounds* **281**, 92–98 (1998).
- [20] N. Li, Q. Huang, X. Y. Yue, S. K. Guang, K. Xia, Y. Y. Wang, Q. J. Li, X. Zhao, H. D. Zhou, and X. F. Sun, “Low-temperature transport properties of the intermetallic compound hoagge with a kagome spin-ice state,” *Phys. Rev. B* **106**, 014416 (2022).
- [21] K. Zhao, Y. Tokiwa, H. Chen, and P. Gegenwart, “Discrete degeneracies distinguished by the anomalous hall effect in a metallic kagome ice compound,” *Nature Physics* **20**, 442–449 (2024).
- [22] Hanbin Deng, Tianyu Yang, Guowei Liu, Lu Liu, Lingxiao Zhao, Wu Wang, Tiantian Li, Wei Song, Titus Neupert, Xiang-Rui Liu, Jifeng Shao, Y. Y. Zhao, Nan Xu, Hao Deng, Li Huang, Yue Zhao, Liyuan Zhang, Jia-Wei Mei, Liusuo Wu, Jiaqing He, Qihang Liu, Chang Liu, and Jia-Xin Yin, “Local excitation of kagome spin ice magnetism seen by scanning tunneling microscopy,” *Phys. Rev. Lett.* **133**, 046503 (2024).
- [23] Paolo Giannozzi, Stefano Baroni, Nicola Bonini, Matteo Calandra, Roberto Car, Carlo Cavazzoni, Davide Ceresoli, Guido L Chiarotti, Matteo Cococcioni, Ismaila Dabo, Andrea Dal Corso, Stefano de Gironcoli, Stefano Fabris, Guido Fratesi, Ralph Gebauer, Uwe Gerstmann, Christos Gougoussis, Anton Kokalj, Michele Lazzeri, Layla Martin-Samos, Nicola Marzari, Francesco Mauri, Riccardo Mazzarello, Stefano Paolini, Alfredo Pasquarello, Lorenzo Paulatto, Carlo Sbraccia, Sandro Scandolo, Gabriele Sclauzero, Ari P Seitsonen, Alexander Smogunov, Paolo Umari, and Renata M Wentzcovitch, “QUANTUM ESPRESSO: a modular and open-source software project for quantum simulations of materials,” *Journal of Physics: Condensed Matter* **21**, 395502 (2009).
- [24] P. Giannozzi, O. Andreussi, T. Brumme, O. Bunau, M. Buongiorno Nardelli, M. Calandra, R. Car, C. Cavazzoni, D. Ceresoli, M. Cococcioni, N. Colonna, I. Carnimeo, A. Dal Corso, S. de Gironcoli, P. Delugas, R. A. DiStasio, A. Ferretti, A. Floris, G. Fratesi, G. Fugallo, R. Gebauer, U. Gerstmann, F. Giustino, T. Gorni, J. Jia, M. Kawamura, H.-Y. Ko, A. Kokalj, E. Küçükbenli, M. Lazzeri, M. Marsili, N. Marzari, F. Mauri, N. L. Nguyen, H.-V. Nguyen, A. Otero de-la Roza, L. Paulatto, S. Poncé, D. Rocca, R. Sabatini, B. Santra, M. Schlipf, A. P. Seitsonen, A. Smogunov, I. Timrov, T. Thonhauser, P. Umari, N. Vast, X. Wu, and S. Baroni, “Advanced capabilities for materials modelling with Quantum ESPRESSO,” *Journal of Physics: Condensed Matter* **29**, 465901 (2017).
- [25] John P. Perdew, Kieron Burke, and Matthias Ernzerhof, “Generalized gradient approximation made simple,” *Phys. Rev. Lett.* **77**, 3865–3868 (1996).
- [26] M.J. van Setten, M. Giantomassi, E. Bousquet, M.J. Verstraete, D.R. Hamann, X. Gonze, and G.-M. Rignanese, “The PseudoDojo: Training and grading a 85 element optimized norm-conserving pseudopotential table,” *Computer Physics Communications* **226**, 39–54 (2018).
- [27] Atsushi Togo and Isao Tanaka, “First principles phonon calculations in materials science,” *Scripta Materialia* **108**, 1–5 (2015).
- [28] E. Kroumova, M. I. Aroyo, J. M. Perez-Mato, A. Kirov, C. Capillas, S. Ivantchev, and H. Wondratschek, “Bilbao crystallographic server: Useful databases and tools for phase-transition studies,” *Phase Transit.* **76**, 155–170 (2003).
- [29] M. I. Aroyo, J. M. Perez-Mato, D. Orobengoa, E. Tasci, G. De La Flor, and A. Kirov, “Crystallography online: Bilbao crystallographic server,” *Bulg. Chem. Commun* **43**, 183–97 (2011).
- [30] Dorian M Hatch and Harold T Stokes, “Invariants: program for obtaining a list of invariant polynomials of the order-parameter components associated with irreducible representations of a space group,” *Journal of applied crystallography* **36**, 951–952 (2003).
- [31] A. P. Cracknell, B. L. Davies, S. C. Miller, and W. F. Love, “Kronecker Product Tables. Vol. 1. General introduction and Tables of irreducible representations of space groups,” (IFI/Plenum, New York, 1979).

- [32] U. Fano, “Effects of configuration interaction on intensities and phase shifts,” *Phys. Rev.* **124**, 1866–1878 (1961).
- [33] S.-F. Wu, W.-L. Zhang, L. Li, H.-B. Cao, H.-H. Kung, A. S. Sefat, H. Ding, P. Richard, and G. Blumberg, “Coupling of fully symmetric As phonon to magnetism in  $\text{Ba}(\text{Fe}_{1-x}\text{Au}_x)_2\text{As}_2$ ,” *Phys. Rev. B* **102**, 014501 (2020).
- [34] D. J. Lockwood and M. G. Cottam, “The spin-phonon interaction in  $\text{FeF}_2$  and  $\text{MnF}_2$  studied by Raman spectroscopy,” *Journal of Applied Physics* **64**, 5876–5878 (1988).
- [35] D. J. Lockwood, “Spin-phonon interaction and mode softening in  $\text{NiF}_2$ ,” *Low Temperature Physics* **28**, 505–509 (2002).
- [36] Qingming Zhang, Ming An, Shikui Yuan, Yong Wu, Dong Wu, Jianlin Luo, Nanlin Wang, Wei Bao, and Yening Wang, “Phonon softening and forbidden mode in  $\text{Na}_{0.5}\text{CoO}_2$  observed by Raman scattering,” *Phys. Rev. B* **77**, 045110 (2008).
- [37] E. Granado, A. García, J. A. Sanjurjo, C. Rettori, I. Torriani, F. Prado, R. D. Sánchez, A. Caneiro, and S. B. Oseroff, “Magnetic ordering effects in the Raman spectra of  $\text{La}_{1-x}\text{Mn}_{1-x}\text{O}_3$ ,” *Phys. Rev. B* **60**, 11879–11882 (1999).
- [38] L. L. Hu, M. Yang, Y. L. Wu, Q. Wu, H. Zhao, F. Sun, W. Wang, Rui He, S. L. He, H. Zhang, R. J. Huang, L. F. Li, Y. G. Shi, and Jimin Zhao, “Strong pseudospin-lattice coupling in  $\text{Sr}_3\text{Ir}_2\text{O}_7$ : Coherent phonon anomaly and negative thermal expansion,” *Phys. Rev. B* **99**, 094307 (2019).
- [39] Ch. Kant, J. Deisenhofer, T. Rudolf, F. Mayr, F. Schrettle, A. Loidl, V. Gnezdilov, D. Wulferding, P. Lemmens, and V. Tsurkan, “Optical phonons, spin correlations, and spin-phonon coupling in the frustrated pyrochlore magnets  $\text{CdCr}_2\text{O}_4$  and  $\text{ZnCr}_2\text{O}_4$ ,” *Phys. Rev. B* **80**, 214417 (2009).
- [40] Karlo Penc, Nic Shannon, and Hiroyuki Shiba, “Half-Magnetization Plateau Stabilized by Structural Distortion in the Antiferromagnetic Heisenberg Model on a Pyrochlore Lattice,” *Phys. Rev. Lett.* **93**, 197203 (2004).
- [41] Doron L. Bergman, Ryuichi Shindou, Gregory A. Fiete, and Leon Balents, “Models of degeneracy breaking in pyrochlore antiferromagnets,” *Phys. Rev. B* **74**, 134409 (2006).
- [42] Fa Wang and Ashvin Vishwanath, “Spin Phonon Induced Collinear Order and Magnetization Plateaus in Triangular and Kagome Antiferromagnets: Applications to  $\text{CuFeO}_2$ ,” *Phys. Rev. Lett.* **100**, 077201 (2008).
- [43] F. A. Gómez Albarracín, D. C. Cabra, H. D. Rosales, and G. L. Rossini, “Spin-phonon induced magnetic order in the kagome ice,” *Phys. Rev. B* **88**, 184421 (2013).
- [44] F A Gómez Albarracín, D C Cabra, H D Rosales, and G L Rossini, “Spin-phonon induced magnetic order in magnetized spin ice systems,” *Journal of Physics: Conference Series* **568**, 042007 (2014).
- [45] Kazushi Aoyama and Hikaru Kawamura, “Spin-lattice-coupled order in heisenberg antiferromagnets on the pyrochlore lattice,” *Phys. Rev. Lett.* **116**, 257201 (2016).
- [46] L. Pili and S. A. Grigera, “Two-dimensional Ising model with Einstein site phonons,” *Phys. Rev. B* **99**, 144421 (2019).
- [47] Masaki Gen and Hidemaro Suwa, “Nematicity and fractional magnetization plateaus induced by spin-lattice coupling in the classical kagome-lattice Heisenberg antiferromagnet,” *Phys. Rev. B* **105**, 174424 (2022).
- [48] Shang Gao, “Dynamic spin-lattice coupling and statistical interpretation for the molecularlike excitations in frustrated pyrochlores,” *Phys. Rev. B* **110**, 214420 (2024).
- [49] Francesco Ferrari, Roser Valentí, and Federico Becca, “Effects of spin-phonon coupling in frustrated Heisenberg models,” *Phys. Rev. B* **104**, 035126 (2021).
- [50] Francesco Ferrari, Federico Becca, and Roser Valentí, “Spin-phonon interactions on the kagome lattice: Dirac spin liquid versus valence-bond solids,” *Phys. Rev. B* **109**, 165133 (2024).
- [51] Sergiy Mankovsky, Hannah Lange, Svitlana Polesya, and Hubert Ebert, “Spin-lattice interaction parameters from first principles: Theory and implementation,” *Phys. Rev. B* **107**, 144428 (2023).
- [52] P. G. Klemens, “Anharmonic decay of optical phonons,” *Phys. Rev.* **148**, 845–848 (1966).
- [53] José Menéndez and Manuel Cardona, “Temperature dependence of the first-order Raman scattering by phonons in Si, Ge, and  $\alpha$ -Sn: Anharmonic effects,” *Phys. Rev. B* **29**, 2051–2059 (1984).